ACS APPLIED MATERIALS & INTERFACES

www.acsami.org

Research Article

Determining Out-of-Plane Hole Mobility in CuSCN via the Time-of-Flight Technique To Elucidate Its Function in Perovskite Solar Cells

Lokeshwari Mohan, Sinclair R. Ratnasingham, Julianna Panidi, Matyas Daboczi, Ji-Seon Kim, Thomas D. Anthopoulos, Joe Briscoe,* Martyn A. McLachlan,* and Theo Kreouzis*

Cite This: ACS Appl. Mater. Interfaces 2021, 13, 38499–38507

Read Online

ACCESS | Metrics & More | Article Recommendations | Supporting Information

ABSTRACT: Copper(I) thiocyanate (CuSCN) is a stable, low-cost, solution-processable p-type inorganic semiconductor used in numerous optoelectronic applications. Here, for the first time, we employ the time-of-flight (ToF) technique to measure the out-of-plane hole mobility of CuSCN films, enabled by the deposition of 4 μm-thick films using aerosol-assisted chemical vapor deposition (AACVD). A hole mobility of $\sim 10^{-3}$ cm^2/V s was measured with a weak electric field dependence of 0.005 cm/V$^{1/2}$. Additionally, by measuring several 1.5 μm CuSCN films, we show that the mobility is independent of thickness. To further validate the suitability of our AACVD-prepared 1.5 μm-thick CuSCN film in device applications, we demonstrate its incorporation as a hole transport layer (HTL) in methylammonium lead iodide ($MAPbI_3$) perovskite solar cells (PSCs). Our AACVD films result in devices with measured power conversion efficiencies of 10.4%, which compares favorably with devices prepared using spin-coated CuSCN HTLs (12.6%), despite the AACVD HTLs being an order of magnitude thicker than their spin-coated analogues. Improved reproducibility and decreased hysteresis were observed, owing to a combination of excellent film quality, high charge-carrier mobility, and favorable interface energetics. In addition to providing a fundamental insight into charge-carrier mobility in CuSCN, our work highlights the AACVD methodology as a scalable, versatile tool suitable for film deposition for use in optoelectronic devices.

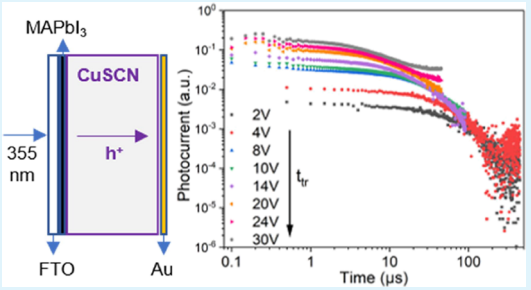

KEYWORDS: *copper(I) thiocyanate, hole transport material, out-of-plane hole mobility, time-of-flight technique, perovskite solar cells*

INTRODUCTION

Since Kojima et al. introduced organic−inorganic halide perovskites as photoactive layers in solar cells, these materials have continued to gain vast interest.[1] Their evolution has been remarkable with device power conversion efficiencies (PCEs) increasing from 3.8% to over 25% in a little over a decade.[1,2] Extensive research has been conducted for improving every aspect of perovskite solar cells (PSCs), including architecture,[3] composition,[4,5] charge-transport layers,[6,7] interlayers,[8,9] and scalability,[10−13] which have resulted in these solar cells being a truly disruptive technology.

A significant area of research has been around identifying alternative hole transport layers (HTLs) to the commonly used organic HTLs that include (2,2′,7,7′-tetrakis(N,N-p-dimethoxyphenylamino)-9,9′-spirobifluorene (spiro-MeOTAD) and poly[bis(4-phenyl)(2,4,6-trimethylphenyl)amine] (PTAA), which yield the highest PCEs.[14−16] The need for alternatives stems from their high cost (>$170 g^{-1}) and low thermal stability, which raise doubts regarding their lifetime and commercial viability.[14,17] Inorganic p-type semiconductors such as copper thiocyanate (CuSCN), copper iodide (CuI), and nickel oxide (NiO) are attractive alternatives because of their relatively low cost (<$10 g^{-1}), dopant-free high conductivity, and high chemical and thermal stability.[18−21] Among these, CuSCN is the most efficient HTL for use in n-i-p architectures.[22] The wide band gap (>3.5 eV), favorable valence-band alignment to $MAPbI_3$ (−5.3 eV), and high field-effect hole mobility ($\sim 10^{-2}$−10^{-1} cm^2/V s) have further made CuSCN an attractive option.[23,24] Moreover, its application is limited to not only conventional (n-i-p) and inverted (p-i-n) PSCs, but also organic solar cells, thin-film transistors, and ultraviolet (UV) photodetectors.[25−31] To optimize the semiconductor for these various applications, it is essential to understand the intrinsic charge-carrier dynamics of CuSCN. To date, values for hole mobility have been obtained via field-effect transistor (FET) measurements and depend on several parameters such as the channel length, dielectric layer, and FET configuration. For example, Pattanasattayavong et al. reported that an order of magnitude lower mobility was measured using CYTOP instead of poly (vinylidene fluoride-trifluoroethylene-chlorofluoroethylene) [P(VDF-TrFE-CFE)]

Received: May 26, 2021
Accepted: July 30, 2021
Published: August 7, 2021

dielectric layers because of Fermi-level pinning at the CuSCN/dielectric interface, which impedes hole transport and influences the final mobility value achieved.[32] Typical undoped FET mobilities for CuSCN are in the range of $\sim 10^{-2}-10^{-1}$ cm^2/V s and increase to 0.3 cm^2/V s when doped.[33,34] However, these FET measurements are not conducted under conditions that represent solar cell performance as they elucidate in-plane mobility, perpendicular to the direction of charge transport in solar cells.

CuSCN as an HTL in PSCs was first reported by Chavhan et al. with devices achieving a PCE of 6.4%.[20] Since then, CuSCN has been incorporated in various n-i-p and p-i-n architectures, resulting in champion PCEs of 20.4 and 16.6%, respectively.[25,35] Because of the ease of processing, CuSCN has been deposited using various techniques, including spin coating,[36,37] spray coating,[38] drop casting,[39] doctor blading,[40] and electrodeposition.[41] Most recently, we have shown that a scalable technique, aerosol-assisted chemical vapor deposition (AACVD), can be used to deposit CuSCN with a minimum thickness of 1.5 μm.[42] Until now, there have been no reports on PSC device performance when AACVD is employed for CuSCN deposition, whereas PCEs have been reported for CuSCN deposited by each of the other techniques stated above, ranging from 6.4% for drop-cast CuSCN to 20.4% for spin-coated CuSCN.[20,25] It should be noted that 20.4% PCE was achieved by incorporating a triple-cation perovskite and reduced graphene oxide interlayer.[25]

As highlighted above, previously reported charge-carrier mobility values calculated from FETs measure in-plane mobility. Time-of-flight (ToF) measurements require thick films for an accurate measurement of the time taken for charge carriers to transit the material. Thus, for the first time, here, we exploit AACVD's unique advantage of creating ultrathick (>1.5 μm) CuSCN films to determine the out-of-plane charge-carrier mobility for two different film thicknesses, which is a more representative value for the direction of charge transport in solar cells. We report the incorporation of 1.5 μm AACVD-deposited CuSCN into n-i-p PSCs, achieving a PCE of 10.4%. In addition to providing a fundamental insight into the charge-transport properties of this intriguing semiconductor material, our results enable us to understand the performance of our AACVD-prepared CuSCN HTLs in PSC devices to determine if they can be used in scalable applications.

To summarize, AACVD is a large-area-scalable fabrication technique for CuSCN, which produces relatively thick films ($\geq$1.5 μm). We observe long-range charge transport in the out-of-plane direction and measure thickness-independent hole mobility of order $\sim 10^{-3}$ cm^2/V s in 1.5 and 4 μm thick films, as well as incorporate the layer in a working PSC. Although the AACVD CuSCN HTL is 75 times thicker than the spin-coated reference CuSCN layer, the PCE shows a very modest drop from 12.6 to 10.4%, demonstrating the excellent charge-transport properties of the high-quality layer produced using the method.

EXPERIMENTAL SECTION

ToF Device Fabrication. Fluorine-doped tin oxide (FTO)-coated glass (2 cm × 2 cm) (TCO 16−15, Solaronix) was used to prepare the ToF devices. Zinc powder and 2 mol dm^{-3} hydrochloric acid (HCl) solution were used to etch the substrates to expose a 1 cm FTO strip at the center of the substrates. The resistivity of the etched area was in the order of MΩ. The substrates were washed with a detergent, acetone, and isopropanol and dried using N_2 prior to UV−ozone cleaning for 20 min. For the perovskite layer, a 1.5 mol dm^{-3} $MAPbI_3$ solution was prepared using lead iodide (TCI 99%, LO279) and methylammonium iodide (Greatcell Solar Materials, MS101000) in a mixture of the *N*,*N*-dimethylformamide: dimethyl sulfoxide solvent at a ratio of 9:1 in a N_2-filled glovebox. The solution was stirred at 60 °C for 2 h and filtered prior to spin coating. The $MAPbI_3$ solution (50 μL) (1.5 mol dm^{-3}) was spun at 4000 rpm for 15 s in a N_2-filled glovebox, and the diethyl ether antisolvent was added 7 s prior to spin coating. Films were annealed at 60 °C for 1 min and 100 °C for 10 min. To form 1.5 and 4 μm CuSCN layers for ToF, filtered 20 and 40 mL solutions of 35 mg/mL CuSCN (99%, Sigma-Aldrich) in diethyl sulfide (DES 98%, Sigma-Aldrich) were deposited in a custom-made AACVD reactor in a well-ventilated fume hood at 60 °C and a N_2 flow rate of 0.5 dm^3/min.[42] Full details are reported in a previous study.[42] Gold (Au) (100 nm) was thermally evaporated to form the counter electrode. ToF devices 1 and 2 are built on a common 4 μm CuSCN layer substrate, whereas devices 3, 4, and 5 are formed on a 1.5 μm CuSCN layer substrate.

ToF Device Testing. The ToF setup (Figure S1) consisted of an excitation source, a sample holder, a signal generator, and an oscilloscope. The excitation source was a frequency-tripled Big Sky Nd: YAG laser (355 nm wavelength), with a pulse width of 8 ns, and was directed at the sample at 5 Hz controlled by a Q-switch. To apply a bias on the sample, an Aim-TTi TGA 1241 (2−10 V) and BNC 6040 universal power generator (10−30 V) were used to generate the voltage pulse. The bias was applied in pulsed mode as it is difficult to discern the transit time using direct current (DC) field because of increased ionic drift screening charges. The voltage drop across a 50 Ω resistor was monitored, and the resulting signals were collected using a Wavesurfer 3024 oscilloscope. An example of the timing sequence and typical currents can be found in Figure S2a. For improved accuracy, an average of 64 signals was calculated. The background current was subtracted from the final data (Figure S2b). To determine hole mobility, the illuminated FTO was biased positive. The ToF sample holder consisted of 5 pins, 4 for each of the gold contacts and 1 which is in contact with the underlying FTO layer. The sample was mounted face down to be in contact with the pins, and the holder was sealed under vacuum. The sample was mounted such that the laser enters through the glass side of the device, and the setup is connected to the signal generator and oscilloscope. The measurements were conducted at room temperature.

Solar Cell Fabrication. Prepatterned FTO-coated glass substrates (1.2 cm × 1.2 cm) (TCO 10−10, Solaronix) were washed sequentially with a detergent, acetone, and isopropanol and then dried under a flow of N_2. The substrates were subjected to UV−ozone cleaning for 20 min before deposition of 40 nm compact and ∼150 nm mesoporous titanium dioxide (TiO_2) electron-transport layers (ETLs). The compact TiO_2 layer was formed by spin coating a solution of 0.2 mol dm^{-3} titanium(IV) isopropoxide (99%, Sigma-Aldrich) and 0.02 mol dm^{-3} HCl in ethanol at 5000 rpm for 60 s, followed by heating at 120 °C for 10 min. The same spin-coating parameters were used to deposit the mesoporous TiO_2 layer using a solution of 18-NRT titania paste (27 wt %, Sigma-Aldrich) diluted in ethanol at a ratio of 1:7 wt % with subsequent annealing at 500 °C for 1 h. For the ∼400 nm perovskite layer, 30 μL of 1.5 mol dm^{-3} filtered $MAPbI_3$ solution was spun onto substrates at 4000 rpm for 15 s, with an addition of 400 μL of diethyl ether antisolvent 7 s prior to spin coating. Substrates were then annealed at 60 °C for 1 min and 100 °C for 10 min. For the AACVD preparation of the HTL, a 20 mL solution of 35 mg/mL CuSCN in DES was prepared and stirred overnight. The solution was filtered prior to deposition. Deposition was conducted at 60 °C, and a N_2 flow rate of 0.5 dm^3/min was used.[42] Postdeposition, substrates were transferred to a N_2-filled glovebox and left for 12 h to dry. Finally, 100 nm counter electrode Au was thermally evaporated onto the substrates. To enable comparison, CuSCN films were also prepared by spin coating; here, 35 μL of 35 mg/mL CuSCN in DES was deposited onto the $MAPbI_3$ layer via dynamic spin coating at 5000 rpm for 30 s.

Solar Cell Testing. PSCs were stored in a N_2-filled glovebox prior to testing. Current density−voltage (J-V) measurements were

https://doi.org/10.1021/acsami.1c09750
ACS Appl. Mater. Interfaces 2021, 13, 38499−38507

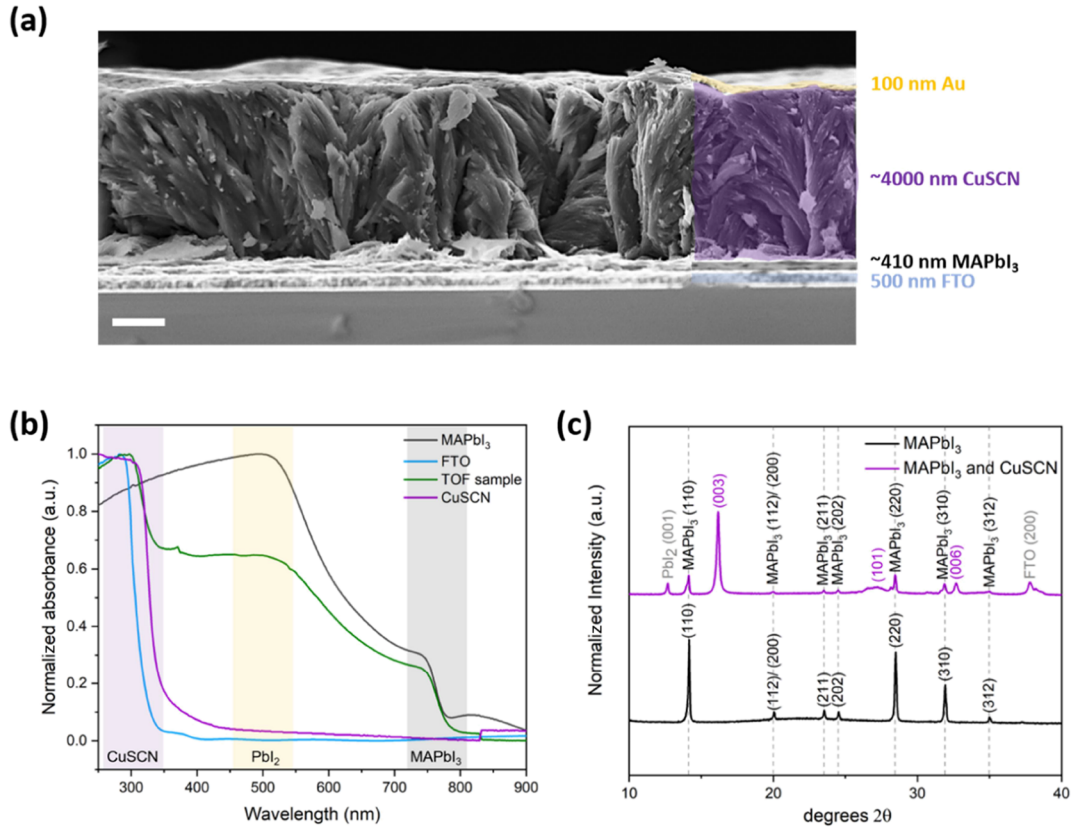

Figure 1. (a) Cross-sectional SEM image (scale bar = 1 μm), (b) UV−vis absorption spectra, and (c) indexed XRD patterns for $MAPbI_3$ and 4 μm CuSCN on $MAPbI_3$.

conducted using a Keithley 2400 source meter. PSCs were illuminated during testing using an AM 1.5 filtered xenon lamp (Oriel instruments) at 100 mW/cm^2 calibrated using a Si reference photodiode. PSCs were scanned in the forward and reverse directions at a rate of 30 mV s^{-1}.

Materials and Device Characterization. Scanning electron microscopy (SEM) was used to study the cross-sectional morphology of the devices. Films were coated with 10 nm Cr and imaged via an in-lens detector using a LEO Gemini 1525 field-emission scanning electron microscope operated at 3 kV. Surface roughness and topography were analyzed using an Agilent 5500 atomic force microscope in tapping mode. The data were analyzed using the Gwyddion software. UV−visible (UV−vis) spectra were acquired using a Perkin Elmer Lambda 25 UV−vis spectrometer and analyzed over the range 200−900 nm. Structural properties were determined by X-ray diffraction (XRD) obtained using a PANalytical X'Pert-Pro diffractometer. Valence-band edges (E_v) were obtained from ambient photoemission spectroscopy (APS) measurements using an APS04 system (KP Technology). A linear fit was used in the cube root photoemission plot to determine the value of E_v.

RESULTS AND DISCUSSION

The ToF device architecture is shown in Figure 1a. SEM cross-section images show a uniform 4 μm CuSCN film deposited via AACVD on a ~410 nm $MAPbI_3$ layer. The reason for incorporating a $MAPbI_3$ layer is threefold. First, $MAPbI_3$ acts as a sensitizer layer, absorbing the laser of wavelength 355 nm and generating the charge carriers that drift through the bulk of the thick CuSCN layer to the counter electrode. The optical absorption spectrum (Figure 1b) shows the absorption onset for the different layers in the ToF device. CuSCN exhibits an absorption onset of 320 nm and therefore does not absorb the laser used for ToF measurements (355 nm wavelength), thus requiring the use of a sensitizer layer. Ideally, a small absorption depth and high charge-generation efficiency are needed for ToF.[43] $MAPbI_3$ exhibits an absorption onset of ~770 nm and serves as the source of photogenerated charge carriers. Second, smoother films of CuSCN form on $MAPbI_3$, reducing the thickness error during the final measurement. Through atomic force microscopy (AFM) measurements (Figure S3), it was found that a CuSCN layer with 30% lower root mean square (RMS) roughness (64 nm) was formed on $MAPbI_3$ in comparison to the CuSCN layer deposited on FTO, which exhibited an RMS roughness of 92 nm.[42] Lastly, the addition of $MAPbI_3$ better represents the PSC structure. Based on the absorption coefficient at 355 nm wavelength (~10^5 cm^{-1}, Figure S4), the laser penetrates less than one-fourth of the $MAPbI_3$ thickness (90 nm), indicating that all the light is absorbed within the $MAPbI_3$ layer. The raw absorbance data, absorption coefficient data, and thickness information for the different material layers can be found in the Supporting Information Figure S4 and Table S1. Therefore, charge generation is limited to the $MAPbI_3$ sensitizer layer. The $MAPbI_3$ and CuSCN layers are sandwiched between two electrodes, FTO and Au (Figure 1a). Short laser pulses are used to generate charge carriers in the $MAPbI_3$ layer, with holes transferred to CuSCN because of the conduction-band offset. To identify the hole mobility in CuSCN, the FTO is biased positive so that the photogenerated holes drift toward the Au counter electrode.[44] The time taken for holes to drift across the bulk thickness (d) of CuSCN at each applied bias (V) is identified as the transit time (t_{tr}) and is used to calculate the mobility (μ) according to eq 1.

https://doi.org/10.1021/acsami.1c09750
ACS Appl. Mater. Interfaces 2021, 13, 38499−38507

$$\mu = \frac{d^2}{t_{tr}V} \quad (1)$$

The absorption spectrum (Figure 1b) also indicates the presence of lead iodide (PbI_2), a degradation product of $MAPbI_3$ (indicated by the yellow region, ~500 nm). The sample was analyzed using XRD to confirm this (Figure 1c, Figure S5). The XRD patterns indicate the presence of some PbI_2 along with the main peaks corresponding to $MAPbI_3$, CuSCN, and FTO. This degradation may have occurred when the devices were exposed to air during the transfer of samples to conduct measurements and because of the longer deposition timeframe required to deposit 4 μm CuSCN. It should be noted that the presence of PbI_2 does not influence the ToF measurement as the measurement only requires sufficient charge carriers to be generated by $MAPbI_3$ to be detected after transit through the CuSCN layer.

For the 4 μm CuSCN device, ToF measurements were conducted over a range of 2−30 V. Typical ToF transients plotted on a double logarithmic scale measured at 5, 10, and 20 V are shown in Figure 2a−c; they indicate the general trend of decreasing t_{tr} with increasing bias. The complete range of ToF transients is shown in Figure S6.

As it is difficult to identify the location of t_{tr} in the linear plot (Figure 2 insets), a double logarithmic plot was used to identify t_{tr}. The t_{tr} value was obtained from the intersection of the linear regions shown in Figure 2a−c. Figure 2a−c shows a decrease in t_{tr} from 35 to 7 μs, with an increase in voltage from 5 to 20 V. The trend follows what is expected because an increase in the electric field should result in the charge carriers drifting through the bulk at a higher speed. To determine the effect of altering the film thickness on the out-of-plane hole mobility, additional ToF measurements were conducted on three 1.5 μm CuSCN film devices over a range of electric fields comparable to the 4 μm film measurements.

Poole−Frenkel plots (Figure 3a,b) are used to identify the relationship between the CuSCN hole mobility and applied electric field. Figure 3a indicates that a CuSCN hole mobility of ~10^{-3} cm^2/V s is reproducibly measured across devices with varying thicknesses of 4 and 1.5 μm CuSCN with weak field dependence at lower electric fields. The effect of higher electric fields on CuSCN hole mobility is analyzed (Figure 3b). Here, a slight increase in field dependence can be seen at higher electric fields, but mobility remains within the order of 10^{-3} cm^2/V s. The average mobility across the range of electric fields studied can also be calculated using a $1/t_{tr}$ vs V plot and is shown for the 4 μm CuSCN devices in Figure S7.

Poole−Frenkel-type electric field dependence allows the calculation of the electric field dependence parameter (γ) according to eq 2.[45] Mobility, zero-field mobility, and electric field are denoted as μ, μ_0, and E, respectively.

$$\mu = \mu_0 \exp(\gamma\sqrt{E}) \quad (2)$$

Here, μ_0 takes the value 4.3×10^{-4} cm^2/V s, facilitating the calculation of γ via an exponential fit of the data, as shown in Figure 3b (Figure S8), resulting in an average value of 0.005 ± 0.0016 $(cm/V)^{1/2}$ over the range of fields measured. μ_0 is calculated by extrapolating the fit to find the mobility when no electric field is applied. For comparison, the field dependence of CuSCN at room temperature matches that of other HTLs such as PTAA.[46]

Given the overlap between the 1.5 μm data and the 4 μm data shown in Figure 3a, we can conclude that the out-of-plane

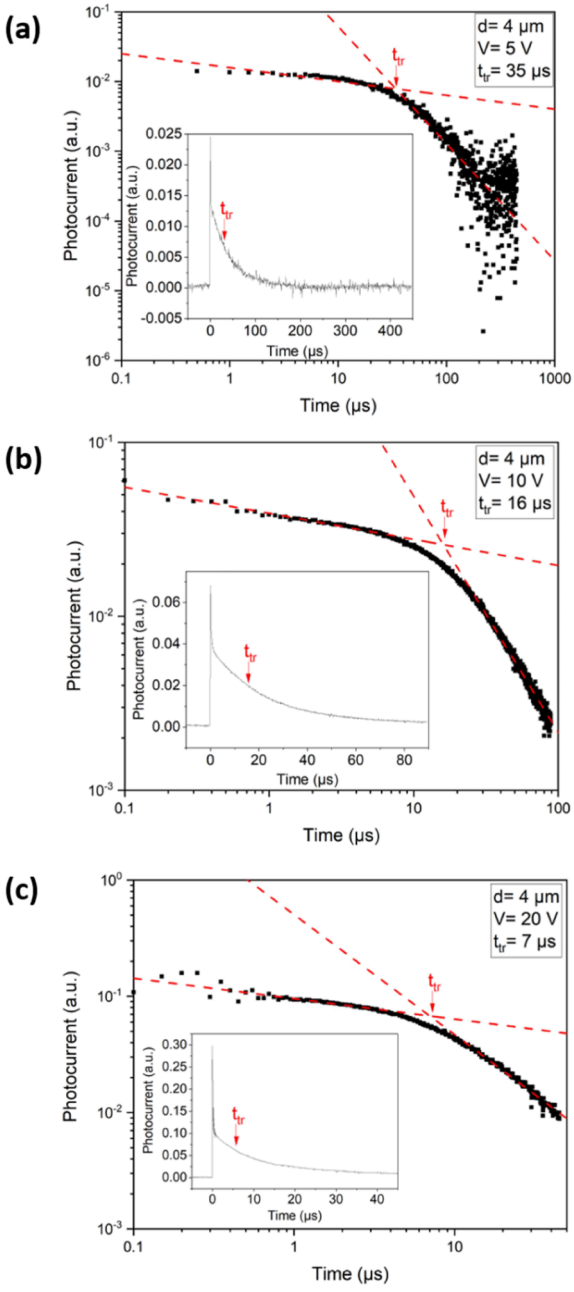

Figure 2. ToF transients measured at different voltages of (a) 5 V, (b) 10 V, and (c) 20 V, plotted on a double logarithmic scale (transit time t_{tr} is indicated on the plots). Insets show the same data plotted on a linear scale.

mobility of AACVD CuSCN is thickness-independent and ~10^{-3} cm^2/V s with a weak field dependence of 0.005 $(cm/V)^{1/2}$. This value is at least an order of magnitude lower than the CuSCN FET mobility values stated in the literature (~10^{-2}−10^{-1} cm^2/V s).[47] It is important to consider that slight differences in mobility do arise from different measurement techniques primarily due to the device geometry.[48] For a more like-for-like comparison, ToF mobilities of commonly used HTLs PTAA and Spiro-OMeTAD have been reported as 10^{-5}−10^{-3} cm^2/V s and 10^{-5}−10^{-4} cm^2/V s, respectively.[46,49,50] Thus, the out-of-plane ToF mobility value we have measured for CuSCN is equal to or higher than the maximum ToF mobility values reported for other HTLs used in PSCs. We conclude that ~10^{-3} cm^2/V s is a more realistic

https://doi.org/10.1021/acsami.1c09750
ACS Appl. Mater. Interfaces 2021, 13, 38499−38507

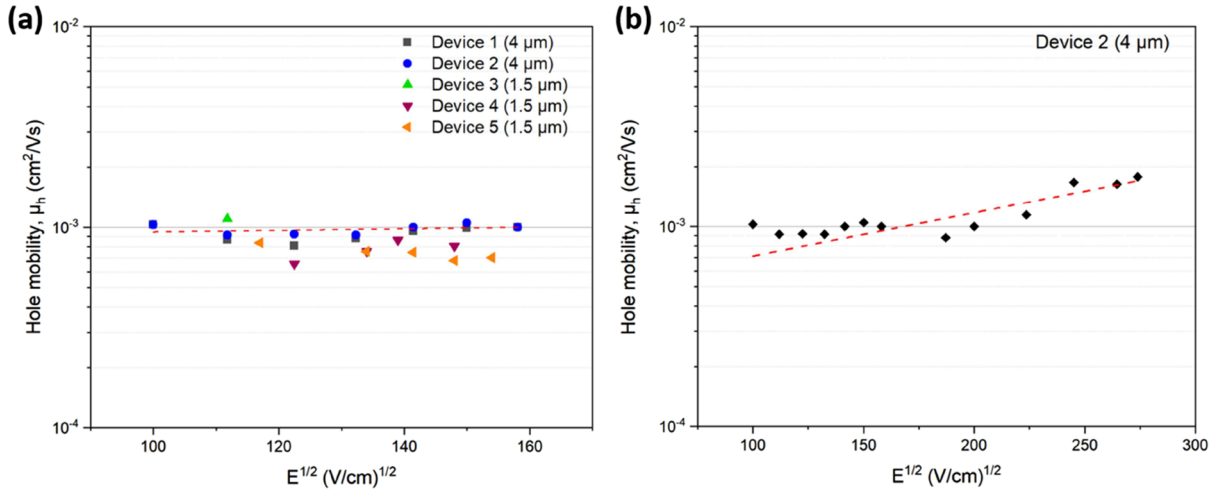

Figure 3. (a) Poole−Frenkel plots for 4 and 1.5 μm CuSCN devices. (b) Device 2 measured across a broad range of electric fields. The dashed line in a and b indicates an exponential fit to the data points of device 2.

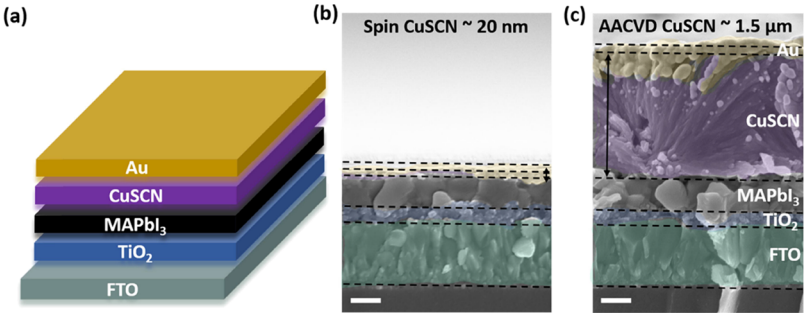

Figure 4. (a) Schematic of the n-i-p PSC structure. (b, c) SEM cross-sections of complete PSCs involving (b) spin-coated and (c) AACVD CuSCN (scale bar = 200 nm).

measurement of CuSCN out-of-plane mobility found in devices than FET mobility measurements.

To investigate how this measured mobility translates to device performance, the performance of CuSCN deposited by AACVD was compared to that of spin-coated CuSCN in PSCs, using n-i-p architectures (Figure 4a). Figure 4b,c shows SEM cross-sections of spin-coated CuSCN and AACVD CuSCN incorporated into PSCs. The SEM images show that the AACVD CuSCN layer is approximately 75 times thicker than the spin-coated CuSCN layer. As previously reported, a thickness of at least 1.5 μm was required to ensure CuSCN films formed by AACVD were continuous and pinhole-free.[42]

Figure 5a,b shows J-V curves and PCE values for each scan direction for the champion spin-coated CuSCN and AACVD CuSCN PSCs. Solar cell parameters for each scan are given in Table 1. Incorporation of AACVD CuSCN in PSCs results in working devices with PCEs of 10.4% in reverse bias and 7.9% in forward bias. In comparison, 20 nm spin-coated CuSCN in the reference cells results in PCEs of 12.6% in reverse bias, but a slightly lower value of 7.5% in forward bias.

The spin-coated CuSCN PSC efficiency is comparable to the reported value of 12.4% PCE for solution-processed CuSCN with the same n-i-p configuration.[40] The absolute drop of only ∼2% PCE indicates that the greater thickness of the AACVD CuSCN layer does not compromise the efficiency as much as may be expected for such a thick HTL layer. This is consistent with the long-range hole transport measured via ToF and proves that AACVD is a promising technique for depositing scalable CuSCN layers. Series and shunt resistance values for champion cells are stated in Table S2. The lower PCE of the AACVD CuSCN device in the reverse scan direction is associated with an increased series resistance of 15.3 Ω cm^2, which is higher than the series resistance of the spin-coated CuSCN device (9.2 Ω cm^2), lowering the fill factor. This indicates that although the mobility of CuSCN is high, the overall conductance of the layer is low due to its thickness. It should be noted that although the AACVD CuSCN layer is 75 times thicker than the spin-coated CuSCN layer, the series resistance has only increased by ∼66%. The increase in shunt resistance for the AACVD CuSCN cell is consistent with the thickness and uniformity of the layer. Through APS measurements, it was found that the E_v of AACVD CuSCN (−5.38 eV) was shallower than that of spin-coated CuSCN (−5.48 eV) and well aligned with the E_v value of $MAPbI_3$ (5.43 eV), which may allow improved charge transfer at the $MAPbI_3$/ AACVD CuSCN interface (Figure 5c, Figure S9).[51] This suggests that the efficiency loss due to the increased series resistance in the AACVD CuSCN may be offset by the improved interfacial energetics. Furthermore, the spin-coated CuSCN cell has a larger hysteresis than the AACVD CuSCN cell. The hysteresis index (HI) is affected by various parameters; however, as in this case, all scans were measured using the same conditions (i.e., identical scan speeds and voltage range), with no previous light soaking, and the HI was calculated using eq 3:[52]

https://doi.org/10.1021/acsami.1c09750
ACS Appl. Mater. Interfaces 2021, 13, 38499−38507

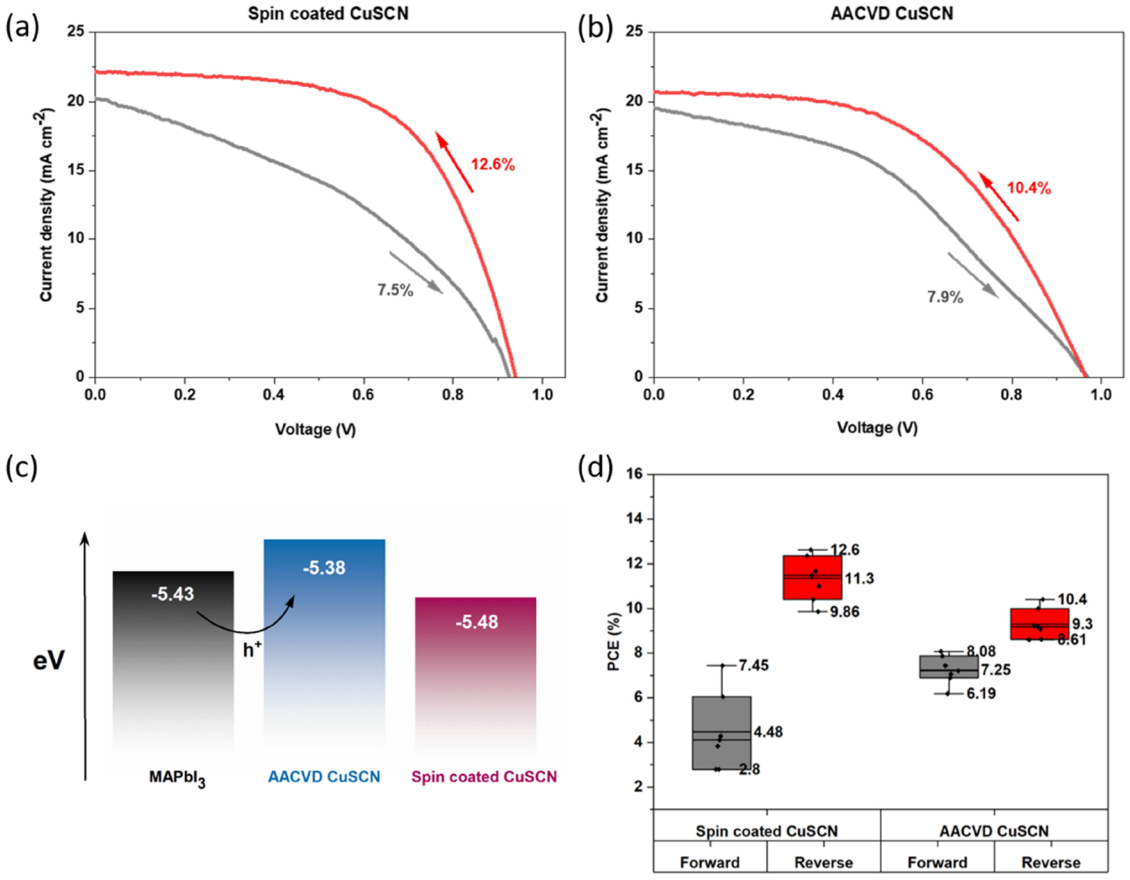

Figure 5. J-V curves of champion cells prepared by (a) spin coating CuSCN (b) and AACVD CuSCN. Energy-level diagram (c) showing ideal valence-band alignment of AACVD CuSCN with $MAPbI_3$ for efficient hole extraction, and (d) shows a boxplot of PCE achieved in the forward and reverse scan directions for seven cells.

Table 1. Summary of Solar Cell Parameters for Champion Cells (Figure 5a,b)

PSC architecture (scan direction)	J_{sc} (mA cm^{-2})	V_{oc} (V)	FF	PCE (%)	HI
FTO/TiO_2/$MAPbI_3$/spin-coated CuSCN/Au (forward)	20.3	0.93	0.40	7.5	0.41
FTO/TiO_2/$MAPbI_3$/spin-coated CuSCN/Au (reverse)	22.1	0.94	0.61	12.6	
FTO/TiO_2/$MAPbI_3$/ AACVD CuSCN/Au (forward)	19.6	0.97	0.42	7.9	0.24
FTO/TiO_2/$MAPbI_3$/ AACVD CuSCN/Au (reverse)	20.7	0.97	0.52	10.4	

$$\text{hysteresis index (HI)} = \frac{\text{PCE (reverse)} - \text{PCE (forward)}}{\text{PCE (reverse)}} \quad (3)$$

Table 1 compares the HI values for cells incorporating the spin-coated and AACVD CuSCN layers. Overall, the AACVD CuSCN layer shows ~40% lower hysteresis. It is known that the redistribution of mobile halide ions originating from $MAPbI_3$ at each of the interfaces screens the built-in field. This impedes charge extraction, leading to hysteresis.[52] However, this effect is reduced using AACVD CuSCN instead of spin-coated CuSCN. Hysteresis has also been linked to interfacial recombination and asymmetry in charge extraction at the HTL and ETL.[53] The improved interfacial energetics of AACVD CuSCN to $MAPbI_3$ leads to efficient hole extraction, reducing interfacial recombination and resulting in decreased hysteresis.

The distribution of PCEs achieved for spin-coated and AACVD CuSCN cells is shown in Figure 5d. The range of PCEs achieved for AACVD CuSCN cells and spin-coated CuSCN cells overlaps in both scan directions, indicating that there are only small differences in performance achieved between the two layer types. The incorporation of AACVD CuSCN results in a lower spreading of data in both scan directions, indicating that it is more reproducible, and the reduced hysteresis can clearly be seen when comparing the full ranges of PCEs achieved in both scan directions.

CONCLUSIONS

For the first time, we have measured an out-of-plane ToF hole mobility for CuSCN, facilitated by the deposition of >1.5 μm CuSCN films by AACVD, giving values of ~10^{-3} cm^2/V s at room temperature with a weak electric field dependence of 0.005 (cm/V)$^{1/2}$. By conducting the ToF measurement using varying film thicknesses of 1.5 and 4 μm CuSCN, we conclude that the mobility is independent of the layer thickness. Although the mobility is lower than CuSCN in-plane FET mobility values stated in the literature, it is equal to or higher than that of other commonly used HTLs such as PTAA and Spiro-OMeTAD measured using ToF. The performance of 1.5 μm CuSCN deposited via AACVD in $MAPbI_3$ PSCs was compared to that of spin-coated CuSCN of 20 nm thickness. PCEs of 10.4% were achieved, which were only slightly lower

https://doi.org/10.1021/acsami.1c09750
ACS Appl. Mater. Interfaces 2021, 13, 38499−38507

than those of spin-coated CuSCN, indicating that the greater thickness of AACVD CuSCN did not compromise the efficiency much. Moreover, a ∼40% decrease in hysteresis was found by incorporating AACVD CuSCN compared with devices using spin-coated CuSCN. This performance is attributed to the high hole mobility and long-range charge transport, with favorable CuSCN/$MAPbI_3$ interfacial properties also identified, which allow efficient hole extraction. These results indicate the potential to use thicker layers of CuSCN in PSCs, which would be more compatible with large-scale processing techniques.

■ ASSOCIATED CONTENT

Supporting Information

The Supporting Information is available free of charge at https://pubs.acs.org/doi/10.1021/acsami.1c09750.

Additional ToF information such as a schematic of ToF setup; sample oscilloscope traces; hole transients ranging 2−30 V for the 4 μm CuSCN sample; alternative method to calculate the hole mobility of CuSCN; additional characterization data such as AFM, UV−vis, XRD, APS data and parasitic solar cell resistance values (PDF)

■ AUTHOR INFORMATION

Corresponding Authors

Joe Briscoe − *School of Engineering and Materials Science and Materials Research Institute, Queen Mary University of London, London E1 4NS, U.K.;* orcid.org/0000-0002-5925-860X; Email: j.briscoe@qmul.ac.uk

Martyn A. McLachlan − *Department of Materials and Centre for Processable Electronics, Imperial College London, Molecular Sciences Research Hub, White City Campus, London W12 0BZ, U.K.;* orcid.org/0000-0003-3136-1661; Email: martyn.mclachlan@imperial.ac.uk

Theo Kreouzis − *School of Physics and Astronomy, Queen Mary University of London, London E1 4NS, U.K.;* orcid.org/0000-0003-2326-5338; Email: t.kreouzis@qmul.ac.uk

Authors

Lokeshwari Mohan − *Department of Materials and Centre for Processable Electronics, Imperial College London, Molecular Sciences Research Hub, White City Campus, London W12 0BZ, U.K.; School of Engineering and Materials Science and Materials Research Institute, Queen Mary University of London, London E1 4NS, U.K.*

Sinclair R. Ratnasingham − *Department of Materials and Centre for Processable Electronics, Imperial College London, Molecular Sciences Research Hub, White City Campus, London W12 0BZ, U.K.; School of Engineering and Materials Science and Materials Research Institute, Queen Mary University of London, London E1 4NS, U.K.*

Julianna Panidi − *Department of Physics and Centre for Processable Electronics, Imperial College London, London SW7 2AZ, U.K.*

Matyas Daboczi − *Department of Physics and Centre for Processable Electronics, Imperial College London, London SW7 2AZ, U.K.;* orcid.org/0000-0001-9920-3657

Ji-Seon Kim − *Department of Physics and Centre for Processable Electronics, Imperial College London, London SW7 2AZ, U.K.;* orcid.org/0000-0003-4715-3656

Thomas D. Anthopoulos − *Division of Physical Sciences and Engineering, King Abdullah University of Science and Technology (KAUST), Thuwal 23955-6900, Saudi Arabia;* orcid.org/0000-0002-0978-8813

Complete contact information is available at: https://pubs.acs.org/10.1021/acsami.1c09750

Notes

The authors declare no competing financial interest.

■ ACKNOWLEDGMENTS

The authors acknowledge EPSRC Centre for Doctoral Training in Plastic Electronic Materials EP/L016702/1 for their support. T.K. wishes to acknowledge STFC (ST/V000039/1) for financial support.

■ REFERENCES

(1) Kojima, A.; Teshima, K.; Shirai, Y.; Miyasaka, T. Organometal Halide Perovskites as Visible-Light Sensitizers for Photovoltaic Cells. *J. Am. Chem. Soc.* **2009**, *131*, 6050−6051.

(2) Best Research-Cell Efficiency Chart| Photovoltaic Research | NREL https://www.nrel.gov/pv/cell-efficiency. html(accessed Jul 15, 2021).

(3) Jena, A. K.; Kulkarni, A.; Miyasaka, T. Halide Perovskite Photovoltaics: Background, Status, and Future Prospects. *Chem. Rev.* **2019**, *119*, 3036−3103.

(4) Suarez, B.; Gonzalez-Pedro, V.; Ripolles, T. S.; Sanchez, R. S.; Otero, L.; Mora-Sero, I. Recombination Study of Combined Halides (Cl, Br, I) Perovskite Solar Cells. *J. Phys. Chem. Lett.* **2014**, *5*, 1628−1635.

(5) Eperon, G. E.; Stranks, S. D.; Menelaou, C.; Johnston, M. B.; Herz, L. M.; Snaith, H. J.; Mhaisalkar, S.; Sum, T. C.; Snaith, H. J.; Moser, J. E.; Grätzel, M.; Park, N.-G. Formamidinium Lead Trihalide: A Broadly Tunable Perovskite for Efficient Planar Heterojunction Solar Cells. *Energy Environ. Sci.* **2014**, *7*, 982.

(6) Le Corre, V. M.; Stolterfoht, M.; Perdigón Toro, L.; Feuerstein, M.; Wolff, C.; Gil-Escrig, L.; Bolink, H. J.; Neher, D.; Koster, L. J. A. Charge Transport Layers Limiting the Efficiency of Perovskite Solar Cells: How To Optimize Conductivity, Doping, and Thickness. *ACS Appl. Energy Mater.* **2019**, *2*, 6280−6287.

(7) Heo, J. H.; Han, H. J.; Kim, D.; Ahn, T. K.; Im, S. H. Hysteresis-Less Inverted CH 3 NH 3 PbI 3 Planar Perovskite Hybrid Solar Cells with 18.1% Power Conversion Efficiency. *Energy Environ. Sci.* **2015**, *8*, 1602−1608.

(8) Deng, W.; Liang, X.; Kubiak, P. S.; Cameron, P. J. Molecular Interlayers in Hybrid Perovskite Solar Cells. *Adv. Energy Mater.* **2018**, *8*, No. 1701544.

(9) Cai, F.; Yang, L.; Yan, Y.; Zhang, J.; Qin, F.; Liu, D.; Cheng, Y.-B.; Zhou, Y.; Wang, T. Eliminated Hysteresis and Stabilized Power Output over 20% in Planar Heterojunction Perovskite Solar Cells by Compositional and Surface Modifications to the Low-Temperature-Processed TiO 2 Layer. *J. Mater. Chem. A* **2017**, *5*, 9402−9411.

(10) Grancini, G.; Roldán-Carmona, C.; Zimmermann, I.; Mosconi, E.; Lee, X.; Martineau, D.; Narbey, S.; Oswald, F.; De Angelis, F.; Graetzel, M.; Nazeeruddin, M. K. One-Year Stable Perovskite Solar Cells by 2D/3D Interface Engineering. *Nat. Commun.* **2017**, *8*, 15684.

(11) Yang, M.; Li, Z.; Reese, M. O.; Reid, O. G.; Kim, D. H.; Siol, S.; Klein, T. R.; Yan, Y.; Berry, J. J.; van Hest, M. F. A. M.; Zhu, K. Perovskite Ink with Wide Processing Window for Scalable High-Efficiency Solar Cells. *Nat. Energy* **2017**, *2*, 17038.

(12) Ono, L. K.; Leyden, M. R.; Wang, S.; Qi, Y. Organometal Halide Perovskite Thin Films and Solar Cells by Vapor Deposition. *J. Mater. Chem. A* **2016**, *4*, 6693−6713.

(13) Mohamad, D. K.; Griffin, J.; Bracher, C.; Barrows, A. T.; Lidzey, D. G. Spray-Cast Multilayer Organometal Perovskite Solar Cells Fabricated in Air. *Adv. Energy Mater.* **2016**, *6*, No. 1600994.

(14) Nair, S.; Gohel, J. V. A Review on Contemporary Hole Transport Materials for Perovskite Solar Cells. In *Green Energy and Technology*. Springer, 2020, 145−168, DOI: 10.1007/978-3-030-33774-2_6.
(15) Li, X.; Bi, D.; Yi, C.; Décoppet, J.-D.; Luo, J.; Zakeeruddin, S. M.; Hagfeldt, A.; Grätzel, M. A Vacuum Flash−Assisted Solution Process for High-Efficiency Large-Area Perovskite Solar Cells. *Science* **2016**, *353*, 58−62.
(16) Bi, C.; Wang, Q.; Shao, Y.; Yuan, Y.; Xiao, Z.; Huang, J. Non-Wetting Surface-Driven High-Aspect-Ratio Crystalline Grain Growth for Efficient Hybrid Perovskite Solar Cells. *Nat. Commun.* **2015**, *6*, 7747.
(17) Pashaei, B.; Bellani, S.; Shahroosvand, H.; Bonaccorso, F. Molecularly Engineered Hole-Transport Material for Low-Cost Perovskite Solar Cells. *Chem. Sci.* **2020**, *11*, 2429−2439.
(18) Patel, S. B.; Patel, A. H.; Gohel, J. V. A Novel and Cost Effective CZTS Hole Transport Material Applied in Perovskite Solar Cells. *Cryst. Eng. Commun.* **2018**, *20*, 7677−7687.
(19) Christians, J. A.; Fung, R. C. M.; Kamat, P. V. An Inorganic Hole Conductor for Organo-Lead Halide Perovskite Solar Cells Improved Hole Conductivity with Copper Iodide. *J. Am. Chem. Soc.* **2014**, *136*, 758−764.
(20) Chavhan, S.; Miguel, O.; Grande, H.-J.; Gonzalez-Pedro, V.; Sánchez, R. S.; Barea, E. M.; Mora-Seró, I.; Tena-Zaera, R. Organo-Metal Halide Perovskite-Based Solar Cells with CuSCN as the Inorganic Hole Selective Contact. *J. Mater. Chem. A* **2014**, *2*, 12754−12760.
(21) Zhu, Z.; Bai, Y.; Zhang, T.; Liu, Z.; Long, X.; Wei, Z.; Wang, Z.; Zhang, L.; Wang, J.; Yan, F.; Yang, S. High-Performance Hole-Extraction Layer of Sol-Gel-Processed NiO Nanocrystals for Inverted Planar Perovskite Solar Cells. *Angew. Chem., Int. Ed.* **2014**, *63*, 12571−12575.
(22) Yin, X.; Song, Z.; Li, Z.; Tang, W. Toward Ideal Hole Transport Materials: A Review on Recent Progress in Dopant-Free Hole Transport Materials for Fabricating Efficient and Stable Perovskite Solar Cells. *Energy Environ. Sci.* **2020**, *13*, 4057−4086.
(23) Er, U.; Icli, K. C.; Ozenbas, M. Spin-Coated Copper(I) Thiocyanate as a Hole Transport Layer for Perovskite Solar Cells. *J. Solid State Electrochem.* **2020**, *24*, 293−304.
(24) Wijeyasinghe, N.; Anthopoulos, T. D. Copper(I) Thiocyanate (CuSCN) as a Hole-Transport Material for Large-Area Opto/Electronics. *Semicond. Sci. Technol.* **2015**, *30*, No. 104002.
(25) Arora, N.; Dar, M. I.; Hinderhofer, A.; Pellet, N.; Schreiber, F.; Zakeeruddin, S. M.; Grätzel, M. Perovskite Solar Cells with CuSCN Hole Extraction Layers Yield Stabilized Efficiencies Greater than 20%. *Science* **2017**, *358*, 768−771.
(26) Treat, N. D.; Yaacobi-Gross, N.; Faber, H.; Perumal, A. K.; Bradley, D. D. C.; Stingelin, N.; Anthopoulos, T. D. Copper Thiocyanate: An Attractive Hole Transport/Extraction Layer for Use in Organic Photovoltaic Cells. *Appl. Phys. Lett.* **2015**, *107*, No. 013301.
(27) Yaacobi-Gross, N.; Treat, N. D.; Pattanasattayavong, P.; Faber, H.; Perumal, A. K.; Stingelin, N.; Bradley, D. D. C.; Stavrinou, P. N.; Heeney, M.; Anthopoulos, T. D. High-Efficiency Organic Photovoltaic Cells Based on the Solution-Processable Hole Transporting Interlayer Copper Thiocyanate (CuSCN) as a Replacement for PEDOT: PSS. *Adv. Energy Mater.* **2015**, *5*, No. 1401529.
(28) Fakharuddin, A.; Vasilopoulou, M.; Soultati, A.; Haider, M. I.; Briscoe, J.; Fotopoulos, V.; Di Girolamo, D.; Davazoglou, D.; Chroneos, A.; Yusoff, A. R. B. M.; Abate, A.; Schmidt-Mende, L.; Nazeeruddin, M. K. Robust Inorganic Hole Transport Materials for Organic and Perovskite Solar Cells: Insights into Materials Electronic Properties and Device Performance. *Sol. RRL* **2021**, *5*, No. 2000555.
(29) Petti, L.; Pattanasattayavong, P.; Lin, Y.-H.; Münzenrieder, N.; Cantarella, G.; Yaacobi-Gross, N.; Yan, F.; Tröster, G.; Anthopoulos, T. D. Solution-Processed p-Type Copper(I) Thiocyanate (CuSCN) for Low-Voltage Flexible Thin-Film Transistors and Integrated Inverter Circuits. *Appl. Phys. Lett.* **2017**, *110*, 113504.
(30) Hatch, S. M.; Briscoe, J.; Dunn, S. A Self-Powered ZnO-Nanorod/CuSCN UV Photodetector Exhibiting Rapid Response. *Adv. Mater.* **2013**, *25*, 867−871.
(31) Li, S.; Guo, D.; Li, P.; Wang, X.; Wang, Y.; Yan, Z.; Liu, Z.; Zhi, Y.; Huang, Y.; Wu, Z.; Tang, W. Ultrasensitive, Superhigh Signal-to-Noise Ratio, Self-Powered Solar-Blind Photodetector Based on n -Ga 2 O 3/p -CuSCN Core−Shell Microwire Heterojunction. *ACS Appl. Mater. Interfaces* **2019**, *11*, 35105−35114.
(32) Pattanasattayavong, P.; Mottram, A. D.; Yan, F.; Anthopoulos, T. D. Study of the Hole Transport Processes in Solution-Processed Layers of the Wide Bandgap Semiconductor Copper(I) Thiocyanate (CuSCN). *Adv. Funct. Mater.* **2015**, *25*, 6802−6813.
(33) Wijeyasinghe, N.; Regoutz, A.; Eisner, F.; Du, T.; Tsetseris, L.; Lin, Y.-H.; Faber, H.; Pattanasattayavong, P.; Li, J.; Yan, F.; McLachlan, M. A.; Payne, D. J.; Heeney, M.; Anthopoulos, T. D. Copper(I) Thiocyanate (CuSCN) Hole-Transport Layers Processed from Aqueous Precursor Solutions and Their Application in Thin-Film Transistors and Highly Efficient Organic and Organometal Halide Perovskite Solar Cells. *Adv. Funct. Mater.* **2017**, *27*, No. 1701818.
(34) Ji, Y.; Lee, H. J.; Lee, S.; Cho, K. G.; Lee, K. H.; Hong, K. High-Performance P-Type Copper(I) Thiocyanate Thin Film Transistors Processed from Solution at Low Temperature. *Adv. Mater. Interfaces* **2019**, *6*, No. 1900883.
(35) Ye, S.; Sun, W.; Li, Y.; Yan, W.; Peng, H.; Bian, Z.; Liu, Z.; Huang, C. CuSCN-Based Inverted Planar Perovskite Solar Cell with an Average PCE of 15.6%. *Nano Lett.* **2015**, *15*, 3723−3728.
(36) Zhao, K.; Munir, R.; Yan, B.; Yang, Y.; Kim, T.; Amassian, A. Solution-Processed Inorganic Copper(I) Thiocyanate (CuSCN) Hole Transporting Layers for Efficient p−i−n Perovskite Solar Cells. *J. Mater. Chem. A* **2015**, *3*, 20554−20559.
(37) Perumal, A.; Faber, H.; Yaacobi-Gross, N.; Pattanasattayavong, P.; Burgess, C.; Jha, S.; McLachlan, M. A.; Stavrinou, P. N.; Anthopoulos, T. D.; Bradley, D. D. C. High-Efficiency, Solution-Processed, Multilayer Phosphorescent Organic Light-Emitting Diodes with a Copper Thiocyanate Hole-Injection/Hole-Transport Layer. *Adv. Mater.* **2015**, *27*, 93−100.
(38) Hatch, S. M.; Briscoe, J.; Dunn, S. Improved CuSCN−ZnO Diode Performance with Spray Deposited CuSCN. *Thin Solid Films* **2013**, *531*, 404−407.
(39) Li, X.; Zhou, D.; Hao, H.; Chen, H.; Weng, Y.; Bian, H. Vibrational Relaxation Dynamics of a Semiconductor Copper(I) Thiocyanate (CuSCN) Film as a Hole-Transporting Layer. *J. Phys. Chem. Lett.* **2020**, *11*, 548−555.
(40) Qin, P.; Tanaka, S.; Ito, S.; Tetreault, N.; Manabe, K.; Nishino, H.; Nazeeruddin, M. K.; Grätzel, M. Inorganic Hole Conductor-Based Lead Halide Perovskite Solar Cells with 12.4% Conversion Efficiency. *Nat. Commun.* **2014**, *5*, 3834.
(41) Ghosh, S.; Sarkar, S. K. Controlled Morphology of Electrochemically Deposited CuSCN by Variation of Applied Bias Voltage. *Energy Procedia* **2014**, *54*, 777−781.
(42) Mohan, L.; Ratnasingham, S. R.; Panidi, J.; Anthopoulos, T. D.; Binions, R.; McLachlan, M. A.; Briscoe, J. Low Temperature Scalable Deposition of Copper(I) Thiocyanate Films via Aerosol-Assisted Chemical Vapor Deposition. *Cryst. Growth Des.* **2020**, *20*, 5380−5386.
(43) Liu, S.-W.; Lee, C.-C.; Su, W.-C.; Yuan, C.-H.; Lin, C.-F.; Chen, K.-T.; Shu, Y.-S.; Li, Y.-Z.; Su, T.-H.; Huang, B.-Y.; Chang, W.-C.; Liu, Y.-H. Downscaling the Sample Thickness to Sub-Micrometers by Employing Organic Photovoltaic Materials as a Charge-Generation Layer in the Time-of-Flight Measurement. *Sci. Rep.* **2015**, *5*, 10384.
(44) Kreouzis, T.; Poplavskyy, D.; Tuladhar, S. M.; Campoy-Quiles, M.; Nelson, J.; Campbell, A. J.; Bradley, D. D. C. Temperature and Field Dependence of Hole Mobility in Poly (9,9-Dioctylfluorene). *Phys. Rev. B* **2006**, *73*, No. 235201.
(45) Bässler, H. Charge Transport in Disordered Organic Photoconductors a Monte Carlo Simulation Study. *Phys. Status Solidi* **1993**, *175*, 15−56.

(46) Barard, S.; Heeney, M.; Chen, L.; Cölle, M.; Shkunov, M.; McCulloch, I.; Stingelin, N.; Philips, M.; Kreouzis, T. Separate Charge Transport Pathways Determined by the Time of Flight Method in Bimodal Polytriarylamine. *J. Appl. Phys.* **2009**, *105*, No. 013701.
(47) Pattanasattayavong, P.; Yaacobi-Gross, N.; Zhao, K.; Ndjawa, G. O. N.; Li, J.; Yan, F.; O'Regan, B. C.; Amassian, A.; Anthopoulos, T. D. Hole-Transporting Transistors and Circuits Based on the Transparent Inorganic Semiconductor Copper(I) Thiocyanate (CuSCN) Processed from Solution at Room Temperature. *Adv. Mater.* **2013**, *25*, 1504−1509.
(48) Myronov, M. Molecular Beam Epitaxy of High Mobility Silicon, Silicon Germanium and Germanium Quantum Well Heterostructures. In *Molecular Beam Epitaxy*; Elsevier, 2018, 37−54, DOI: 10.1016/B978-0-12-812136-8.00003-7.
(49) Poplavskyy, D.; Nelson, J. Nondispersive Hole Transport in Amorphous Films of Methoxy-Spirofluorene-Arylamine Organic Compound. *J. Appl. Phys.* **2003**, *93*, 341−346.
(50) Meng, G.; Shi, Y.; Song, X.; Ji, M.; Xue, Y.; Hao, C. Theoretical Insight into the Carrier Mobility Anisotropy of Hole Transport Material Spiro-OMeTAD. *Curr. Appl. Phys.* **2017**, *17*, 1316−1322.
(51) Daboczi, M.; Kim, J.; Lee, J.; Kang, H.; Hamilton, I.; Lin, C.; Dimitrov, S. D.; McLachlan, M. A.; Lee, K.; Durrant, J. R.; Kim, J.-S. Towards Efficient Integrated Perovskite/Organic Bulk Heterojunction Solar Cells: Interfacial Energetic Requirement to Reduce Charge Carrier Recombination Losses. *Adv. Funct. Mater.* **2020**, *30*, No. 2001482.
(52) Habisreutinger, S. N.; Noel, N. K.; Snaith, H. J. Hysteresis Index: A Figure without Merit for Quantifying Hysteresis in Perovskite Solar Cells. *ACS Energy Lett.* **2018**, *3*, 2472−2476.
(53) Calado, P.; Telford, A. M.; Bryant, D.; Li, X.; Nelson, J.; O'Regan, B. C.; Barnes, P. R. F. Evidence for Ion Migration in Hybrid Perovskite Solar Cells with Minimal Hysteresis. *Nat. Commun.* **2016**, *7*, 13831.

https://doi.org/10.1021/acsami.1c09750
ACS Appl. Mater. Interfaces 2021, 13, 38499−38507